CEAS Space Journal
https://doi.org/10.1007/s12567-025-00650-7

ORIGINAL PAPER

Simulating the interaction between a free-flying ring and a curved shock wave: DLR results of the ESA ATD3-Workshop 2022

Bodo Reimann[1]

Received: 31 October 2024 / Revised: 27 June 2025 / Accepted: 16 July 2025
© The Author(s) 2025

Abstract

A free-flying ring crossing the curved bow shock in front of cylinder was selected as numerical test case within ESA's Aerothermodynamics and Design for Demise working group in 2022. The experiment to compare with was carried out in the VKI Longshot gun tunnel facility at a free stream Mach number of about 14. This paper presents the DLR simulation results achieved by coupling the DLR in-house CFD solver TAU with a 6-DoF flight mechanic solver. Local dynamic grid adaptation is used to capture shocks and unsteady shock interactions. The results of the coupled simulation are compared to results of a simulation with prescribed motion using the experimental determined motion state as input, and to results of a flight mechanic simulation prescribing the measured aerodynamic forces and moments. Both the coupled and the forced motion simulation show similar values for the aerodynamic loads but higher than the measured ones. The flight mechanic simulation shows good agreement with the VKI experiments.

Keywords CFD 6-DoF coupling · Space debris · Free-flight modeling · Shock interaction · ATD3-workshop

Abbreviations

6-DoF	Six degree of freedom
ATD3	Aerothermodynamics and design for demise
CFD	Computational fluid dynamics
CoG	Center of gravity
DLR	German Aerospace Center
RBD	Rigid body dynamics
VKI	von Karman Institute for Fluid Dynamics

Subscripts

∞	Free stream values
exp	Measured value
sim	Simulated value

Greek

α	Angle of attack
$\dot{\vec{\phi}}$	Rotation rate vector $\dot{\vec{\phi}} = (p, q, r)$
ρ	Density
$\vec{\phi}$	Orientation vector $\vec{\phi} = (\phi, \theta, \psi)$

Greek

$\bar{I}$	Inertia tensor $\bar{I} = I_{ij}$
$\dot{\vec{x}}$	Velocity vector $\dot{\vec{x}} = (u, v, w)$
$\vec{F}$	Force vector $\vec{F} = (F_x, F_y, F_z)$
$\vec{g}$	Gravitational acceleration
$\vec{M}$	Moments vector $\vec{M} = (M_x, M_y, M_z)$
$\vec{x}$	Position vector $\vec{x} = (x, y, z)$
C_D	Drag coefficient
C_L	Lift coefficient
C_m	Pitching moment coefficient
C_p	Pressure coefficient
D	Drag
h	Height
L	Lift
M	Mach number
m	Mass
R	Radius
T	Temperature
t	Time, thickness

1 Introduction

Discarded parts of past space missions remain in orbit for long periods of time before they enter the atmosphere uncontrolled, burn up, or partially hit the surface. These broken

---

✉ Bodo Reimann
bodo.reimann@dlr.de

[1] Institute of Aerodynamics and Flow Technology, Spacecraft, German Aerospace Center (DLR), Lilienthalplatz 7, Braunschweig, Germany

Published online: 18 August 2025

satellites, burnt out rocket stages, lost tool boxes or paint chips form a growing cloud of space debris around our planet. The size of the parts ranges from several meters to centimeters down to the fraction of a millimeter. Cascading collisions between these objects create new, smaller debris which in turn increase the likelihood of further collisions (Kessler effect). Even the tiniest parts possess huge kinetic energy due to their tremendous speed, and may cause great damage in case of a collision with an active mission. In short, the garbage becomes a growing problem for space travel. The goal for the future must be to avoid further space debris. One way is to initiate the re-entry after the end of the operational period, with a structural design that ensures the demise. The purpose of a design for demise is to break apart the structure and burn its components due to the high mechanical and thermal stresses during the re-entry. Software tools that can compute re-entry trajectories and possible ground footprints rely on simplified aerodynamic methods and correlations. These tools are restricted to simple geometries and do not take into account the interaction between different fragments and shock waves. For a better understanding of these effects the Aerothermodynamics & Design for Demise (ATD3) working group test case 2022 focuses on the aerodynamic behaviour and prediction of interacting free-flying bodies at hypersonic speed.

2 Test case description and experimental set-up

The selected test case consists of a free-flying annular ring crossing the oblique bow shock in front of a two-dimensional fixed cylinder. The test has been carried out in the VKI Longshot hypersonic gun tunnel using free-flight measurement technique at a free stream Mach number of 14. The scenario represents a generic interaction between an inter-stage adapter and a rocket stage during break-up and reentry. The experimental set-up and the results are discussed in detail by Kovács et al. [1] and [2]. Figure 1 shows the Longshot test section with the nozzle, the cylinder mounted in lateral direction, and the ring suspended by thin wires above the cylinder. When the flow builds up, the wires break and the ring flies freely in the test section and interacts with the oblique shock generated by the cylinder. The test time is in the range of a few milliseconds. During this time a number of schlieren pictures is taken. The trajectory, velocity and acceleration of the ring is reconstructed from the pictures using an optical tracking algorithm. Below the cylinder shown in Fig. 1 a set of probes is installed to measure static pressure and stagnation pressure and heat flux. Using a viscous correction of the measured static pressure, Rankine–Hugoniots jump relation, and Fay–Riddell's formula for stagnation heat flux, the free stream velocity and temperature are iterated from a first guess until they match the measured values [3]. The final test case consists of a data set which contains free stream data, the position, and orientation and all velocities and accelerations of the ring, and the derived aerodynamic coefficients over time. The goal of the workshop was to provide numerical results of the free-flying ring and to compare them with the experimental results.

Fig. 1 Experimental set-up in the VKI Longshot test section (taken from [1])

Both the cylinder and the ring have a outer radius of $R = 60\,mm$. The ring has a height of $h = 15$ mm and a thickness of $t = 2$ mm. With the mass $m = 13.3$ g the tensor of inertia with respect to the Center of gravity (GoG) contains the main moments of inertia on the diagonal

$$I_{yy} = I_{zz} = \frac{m}{12}\left[3\,R^2 + 3(R-t)^2 + h^2\right] \tag{1}$$

$$= 5.548675 \cdot 10^{-6}\ \text{kg}\ \text{m}^2 \tag{2}$$

$$I_{xx} = \frac{m}{2}\left[R^2 + (R-t)^2\right] \tag{3}$$

$$= 11.1986 \cdot 10^{-6}\,\text{kg}\,\text{m}^2 \quad . \tag{4}$$

Since the selected coordinate system coincides with the main axes, the off-diagonal moments disappear

$$I_{xy} = I_{xz} = I_{yz} = 0.0\,\text{kg}\,\text{m}^2 \quad . \tag{5}$$

A detailed analysis of the experiment showed that the wires holding the ring in its initial position did not break immediately with the start-up of the flow [2]. For the test case it was decided to start the numerical simulation at $t = 3.8$ ms after the arrival of the flow in the test section, at this time the ring is free. The motion state and free stream conditions at this time are summarized in Table 1. The complete time-history of free stream data taken from [1] is shown in Fig. 6. The test gas in the VKI facility is to be assumed calorically perfect nitrogen, all body surfaces are modeled as

Table 1 Measured free stream and motion data of the ring [1] used as input for the numerical simulations

t [ms]	u_∞ [m/s]	ρ_∞ [g/m^3]	T_∞ [K]	x [mm]	z [mm]	u [m/s]	w [m/s]	θ [°]	q [°/s]
3.8	2530	5.02	79.9	–33.77	77.43	3.603	0.353	–2.04	–483.75
6.0	2440	5.01	81.4	–24.30	78.36	4.970	0.733	–3.06	–564.13
9.0	2340	4.66	73.0	–6.95	83.84	6.562	3.126	–4.66	–532.28
12.0	2240	4.77	63.9	15.29	96.93	8.291	5.322	–7.63	–1665.02

non-slip isothermal boundaries with constant wall temperature of $T_{\text{wall}} = 300\,\text{K}$. Sutherland's law is used to determine the temperature dependency of the viscosity. The Reynolds number is within the laminar flow regime.

3 Numerical scheme

The presented numerical results have been carried out with the DLR TAU code. The TAU flow solver [4, 5] is a cell centered finite volume method to solve the Euler or Navier-Stokes equations on unstructured grids. Based on a primary grid an edge-based dual-grid metric is generated in a preprocessing step. In the same step coarser levels of the dual-grid are agglomerated to accelerate numerical convergence using the multi-grid technique. Domain splitting is also performed by the preprocessor in order to run parallel computations. In the CFD solver module inviscid terms are computed by employing an AUSMDV upwind scheme using linear reconstruction to get second-order spatial accuracy. Viscous terms are computed with a second-order central scheme. For time integration an explicit Runge-Kutta scheme, as well as an implicit approximate factorization lower-upper symmetric Gauss-Seidel scheme (LU-SGS) are implemented.

In order to perform simulations with moving grids TAU is written in an arbitrary Lagrangian-Eulerian formulation. The technique of overlapping grids [6] (Chimera technique) allows for the simulation of configurations with movable parts. The method handles the data exchange and interpolation in the overlapping regions. Grid regions that overlap solid parts have to be excluded from the flow computation. This is done by an automatic hole cutting procedure [7] which is based on the intersection of grid edges and surface cells to detect grid points inside solid bodies. Data exchange in surface boundary layers may cause interpolation errors due to large gradients and the insufficient resolution of the overlapping grid. To avoid this a procedure to adapt the location of the interpolation zone is implemented in order to minimize the width of the overlap, so that the interpolation boundaries are shifted away from the body surfaces. The current implementation of the Chimera technique covers multiple moving parts, and is also available for parallel simulations.

Grid adaptation allows a local refinement of the mesh by dividing the edges of the primary grid. The flow variables serve as an indicator for the division of the edges. The adaptation module also allows the removal of previously added points based on the indicator. The adaptation is limited by a minimum edge length, a maximum refinement level of the original edge or a maximum number of total grid points.

The motion of bodies under the influence of external forces is separately computed in a Rigid Body Dynamics (RBD) module solving Newton's second law and the Euler equation of rotational dynamics. The equations represent a system of ordinary first-order differential equations which are solved using Newtons's method for time integration. The scheme converges to machine accuracy within five interations [9].

The coupled CFD/RBD problem is solved in a partitioned manner. A so-called strong coupling scheme [8, 9] is used. Strong coupling means that the coupled equations are iteratively solved within every physical time step by repeatedly solving the involved disciplines CFD and RBD separately based on the exchanged coupling quantities. These are on CFD side aerodynamic loads (forces and moments) and on RBD side the motion state (position, rotation angles, velocities, and rotation rates). The coupling scheme performs one predictor and a number of corrector steps. The corrector steps are terminated and the code proceeds to the next physical time step until a given number of corrector steps is reached or the solution update of motion state and loads falls below a predefined threshold [9]. If the number of corrector steps is set to zero, the strong coupling scheme turns into a weak coupling scheme. Figure 2 shows an operation chart of the CFD/RBD coupling.

4 Simulation procedure and computational domain

Three types of numerical simulations have been carried out. A strong coupled CFD/RBD simulation using the TAU CFD solver and the TAU 6-DoF RBD module.

$$\underset{\text{motion state}}{\left(\vec{x},\dot{\vec{x}},\vec{\phi},\dot{\vec{\phi}}\right)_{\text{sim}}} \underset{\text{RBD}}{\overset{\text{CFD}}{\rightleftarrows}} \underset{\text{loads}}{\left(\vec{F},\vec{M}\right)_{\text{sim}}}$$

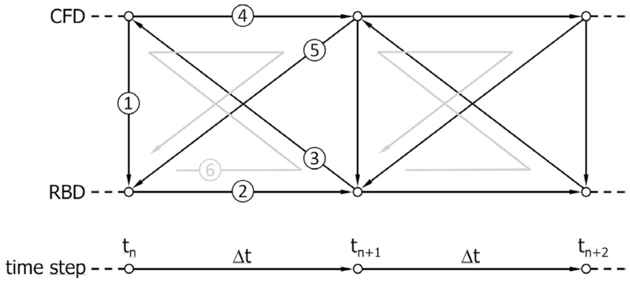

Fig. 2 CFD/RBD coupling scheme. ①, ⑤ exchange of aerodynamic loads, ② computation of RBD time step,③ exchange of motion state, ④ computation of CFD time step, ⑥ repetition of step ① to ④ until convergence

In the forced motion simulation the motion state measured in the VKI experiment is prescribed instead of solving the flight mechanic equations. Aerodynamic loads are then computed using the TAU CFD solver.

$$\left(\vec{x},\dot{\vec{x}},\vec{\phi},\dot{\vec{\phi}}\right)_{\text{exp}} \overset{\text{CFD}}{\rightharpoonup} \left(\vec{F},\vec{M}\right)_{\text{sim}}$$

In the flight mechanic or rigid body simulation, the TAU 6-DoF RBD module computes the motion state using the measured aerodynamic loads as input. The simulation of the flow field is not necessary in this case.

$$\left(\vec{x},\dot{\vec{x}},\vec{\phi},\dot{\vec{\phi}}\right)_{\text{sim}} \underset{\text{RBD}}{\leftharpoondown} \left(\vec{F},\vec{M}\right)_{\text{exp}}$$

In all cases with prescribed data, linear interpolation between the given experimental data is used to generate input data for the smaller computational time step (Fig. 3).

The TAU code calculates all values in the body-fixed coordinate system of the ring. For the comparison the data have to be transformed to the aerodynamic coordinate system. The motion of the ring is not restricted in the simulation, so that the motion state has 12 values three each for position and orientation and three more each for the corresponding velocities. The fully coupled results show that the lateral motion, as well as the roll and yaw rotation are neglectable. For the simulations with prescribed motion or loads these values are zero anyway, as they are not included in the experimental data set. For these reasons only three degrees of motion (longitudinal, vertical, and pitch) will be consider. Lift and drag measured in the wind tunnel coordinate system then result from the body-fixed forces according to

$$D = F_z \sin\theta + F_x \cos\theta \tag{6}$$

$$L = F_z \cos\theta - F_x \sin\theta \tag{7}$$

and the corresponding coefficients are calculated according to

$$C_D = \frac{D}{q_\infty \, 2\,R\,h} \tag{8}$$

$$C_L = \frac{L}{q_\infty \, 2\,R\,h} \tag{9}$$

$$C_m = \frac{M_y}{q_\infty \, 2\,R^2\,h} \quad . \tag{10}$$

In the aerodynamic coordinate system the motion of the ring with respect to the free stream of the wind tunnel has to be considered for the computation of the dynamic pressure q_∞

$$q_\infty = \frac{1}{2}\,\rho_\infty\left[\left(u_\infty - u\right)^2 + w^2\right] \tag{11}$$

and the angle of attack α as sum of the pitch angle θ and the flight path angle γ

$$\alpha = \theta - \gamma \tag{12}$$

with

$$\gamma = \arctan\left(\frac{w}{u_\infty - u}\right) \quad . \tag{13}$$

The pressure coefficient is defined as

$$C_p = \frac{p - p_\infty}{\frac{1}{2}\,\rho_\infty u_\infty^2} \quad . \tag{14}$$

The computational domain shown in Fig. 4 consist of a rectangular box of $225 \times 200 \times 225$ mm. The cylindrical sub-domain for the ring has a radius of 70 mm and height of 95 mm. The ring has the initial position and orientation given in Table 1. The domain is discretized using the commercial grid generation software CENTAUR. The hybrid mesh consists of tetrahedrons and triangular prisms. The boundary layer of the ring is resolved with 32 prismatic layers, that of the cylinder with 40. The wall distance of the first layer is in each case 10^{-3} mm. The initial mesh has around 7.9 million points and is dynamically adapted during the unsteady simulation to a minimum edge length of 0.1 mm and a maximum number of 20 million points. Figure 5 shows on the left-hand side the center plain of the initial grid. On the right-hand side the grid was locally refined to capture shock waves, furthermore regions of the grids that overlap solid bodies have been blanked.

The unsteady coupled and forced motion simulations start from a converged flow field solution on a refined mesh using the initial condition at $t = 3.8$ ms given in Table 1. In each time step the motion state and/or the aerodynamic field is computed depending on the used simulation type. At the end

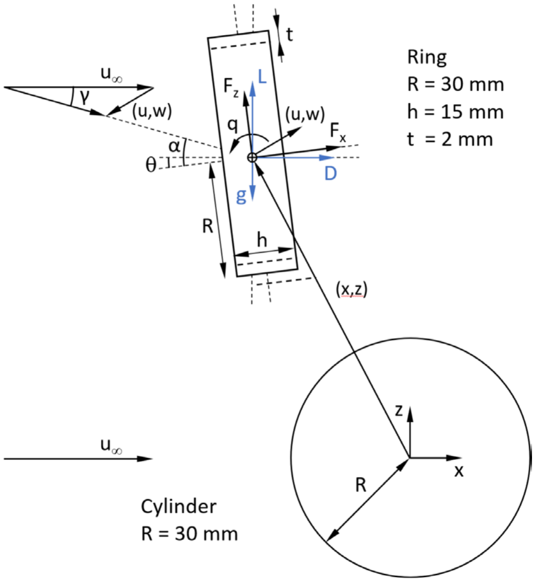

Fig. 3 Dimensions of the configuration and coordinate systems

of the time step the grid is adapted to capture the new shock contours and the inflow condition is updated according to the measured free stream values shown in Fig. 6.

In total 9.2ms of physical time have been simulated from 3.8ms to 13.0ms.

All simulations use a physical time step of $\Delta t = 0.1$ ms. The flight mechanic simulation only computes the motion state. For the coupled simulations 500 inner iteration for the CFD solver and five coupling cycles have been completed. This means one coupled time step consisting of one predictor and five corrector steps requires 3000 iterations. The convergence of the scheme is shown in Fig. 7 for seven physical time steps. The density residual as well as the pitching moment are fully converged within each time step. The results after the first 500 iterations of every time step correspond to the weak coupled solution.

All simulations have been carried out on the DLR HPC Cluster for Advanced Research and Aerodynamics (CARA) in Dresden, the used compute nodes consist of two AMD EPYC 7601 2.2 GHz CPUs with 32 cores each. On 16 nodes the coupled simulation of 92 time steps requires 105h. Each coupling step (predictor or corrector) takes a bit less than 11min the grid adaptation and repartitioning takes around 4min.

A time step convergence study with a time step of $\Delta t = 0.05$ ms shows no difference in the results.

To check the influence of the spatial discretization of the computational domain on the aerodynamic coefficients of the ring steady-state simulations at three times have been performed. The simulations have been made for the ring with and without the cylinder. The flowfield has been computed on two different 3D meshes. The free stream in the cases with cylinder corresponds to the conditions at $t = 6.0$ ms, 9.0 ms, and 12.0 ms. The case without the cylinder correspond to the initial condition at $t = 3.8$ ms but with zero angle of attack to allow the comparison with an axisymmetric computation. Velocity and rotation rate of the ring are zero for this study. The nominal grid is the grid used for the unsteady simulations. The fine grid has more points and quadrilateral prisms in the boundary layer of the ring. The quadrilateral discretization of the ring surface allows a better resolution of the rectangular edges. For the nominal grid the same adaptation strategy as for the unsteady simulation is used. For the adaptation of the fine grid more points are added in each step and the total number of points in not limited. For the axisymmetric grid the first wall distance is between $1.25 \cdot 10^{-4}$ and $2.50 \cdot 10^{-4}$ mm. All steady-state simulation results are summarized in Table 2. The difference is around 3% for the drag and 1% for the lift. At 12.0 ms the wake of the ring becomes unsteady, which leads to deviations of 10% in the pitching moment.

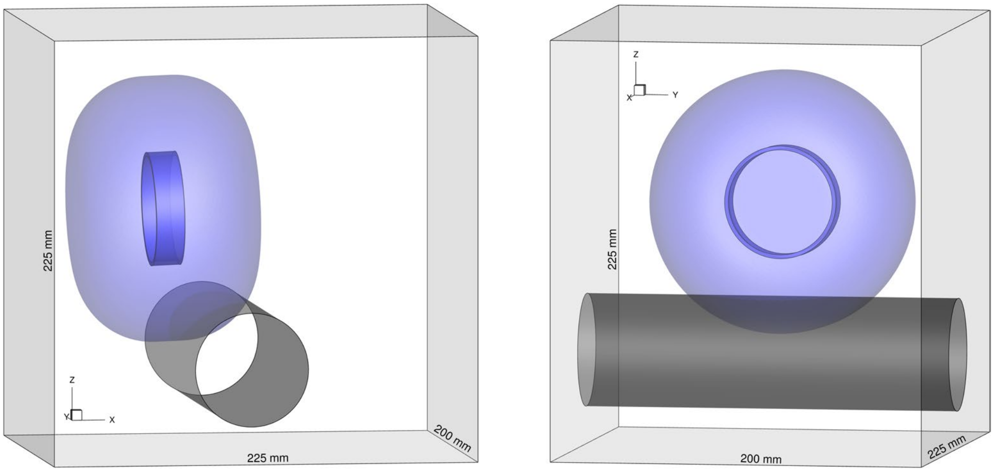

Fig. 4 Computational domain. The domain consists of two overlapping sub-domains for the cylinder (grey) and the ring (blue)

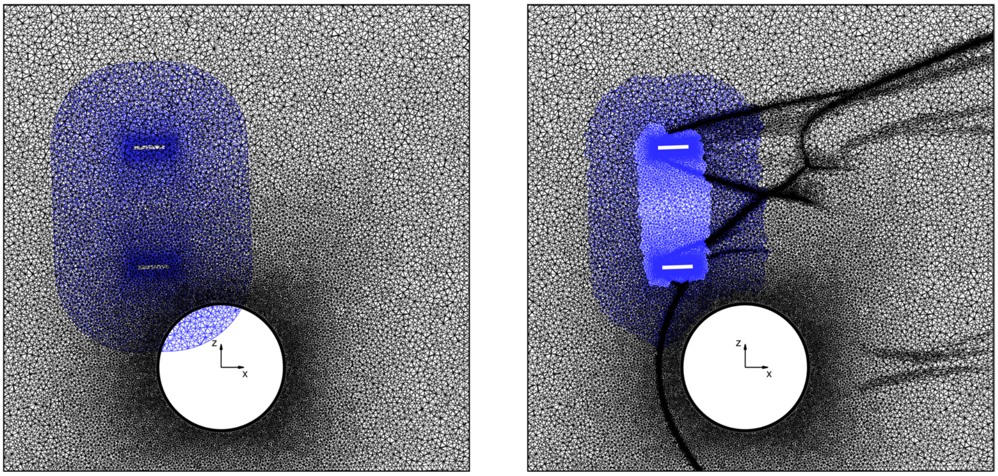

Fig. 5 Center cut-plane of the primary computational mesh. Cylinder mesh with inertial coordinate system (black) and overlapping ring mesh (blue). The picture shows on the left the original mesh, and on the right a local refined mesh where the body overlapping parts have been blanked

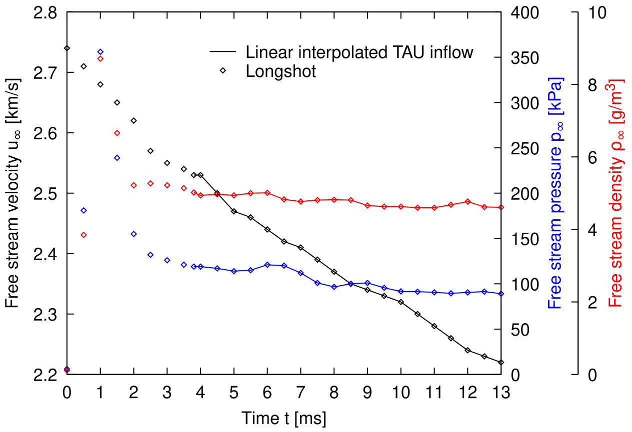

Fig. 6 Time-history of the measured free stream values (data taken from [1]). A linear interpolation is used to determine the TAU inflow boundary condition

5 Results

The results of all simulations and the experiment are compared in Figs. 9 and 10. Figure 9 shows the variation of lift, drag, and pitching moment of the ring versus angle of attack (left) and versus time (right). Figure 10 shows the time-history of horizontal and vertical position, the attitude, and the corresponding velocities of the ring. To illustrate the influence of the shock interaction on the motion and the aerodynamic forces on the ring (blue) additional coupled simulation results without the cylinder (red) are presented. In the case without shock interaction the ring moves with almost uniform acceleration.

During the entire test period the results of the fully coupled CFD/RBD simulation (solid blue lines) show up to 25% higher drag values compared to the measurements. Lift and pitching moment are also above the measured values until they reach their maximum values at $t = 8.3$ ms and $t = 8.1$ ms respectively. The comparison with the simulation without cylinder (solid red lines) shows that the bow shock of the cylinder already has an influence on the ring right at the start of the simulation at $t = 3.8$ ms. The change over time in the experimental values is also less pronounced compared to the computation. Not reproduced by the simulation is the bending of the curves of drag and pitching moment at $t = 11$ ms. The larger simulated forces lead to higher velocities and a greater distance covered by the ring at the same

Table 2 Influence of the spatial resolution on the aerodynamic coefficients of the ring

Grid	No. of points (initial grid)	No. of points (adapted grid)	C_D	C_L	C_m
		Ring w/ cylinder at $t = 12.0$ ms			
3D nominal	7.9M	19.9M	0.87973	0.57963	-0.08215
3D fine	10.8M	82.1	0.90222	0.58191	-0.09006
		Ring w/ cylinder at $t = 9.0$ ms			
3D nominal	7.9M	19.8M	0.77204	1.07820	-0.05052
3D fine	10.8M	82.2M	0.79561	1.07962	-0.05168
		Ring w/ cylinder at $t = 6.0$ ms			
3D nominal	7.9M	19.9M	0.66162	0.76695	-0.00176
3D fine	10.8M	82.3M	0.68381	0.77706	-0.00047
		Ring w/o cylinder at $t = 3.8$ ms but $\alpha = 0°$			
3D nominal	4.3M	11.4M	0.73545	–	–
3D fine	7.2M	54.9M	0.75937	–	–
2.5D	4.1M	6.6M	0.75995	–	–

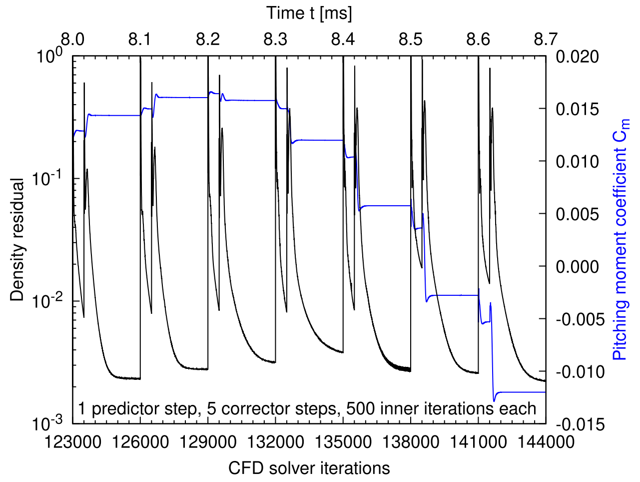

Fig. 7 Density residual and pitching moment coefficient C_m versus the number of CFD solver iterations for seven time steps with strong CFD/RBD coupling

time, the difference in pitching moment leads to a smaller pitch angle as shown in Fig. 10. A different positioning of the ring within the shock layer of the cylinder in turn influences the location and the type of the shock interaction and thus the surface pressure distribution and the acting forces and moments.

To separate these effects the results of a forced motion simulation (dashed blue line) prescribing the measured trajectory are compared in Fig. 9. Considering the distributions of the aerodynamic loads versus time both simulations show very similar results, the differences between the simulations are much smaller than the differences compared to the Longshot data. Considering the loads versus angle of attack the forced motion data show a shift towards higher (negative) angles and are closer to the measured points. The angle of attack is a time dependent variable and the shift is due to the fact that the pitch angle from the forced simulation is always smaller than the pitch angle computed by the coupled simulation. Despite the identical movement of the ring in the forced motion simulation and the experiment the simulated forces are still much higher.

The results of the steady-state computations (circles) are consistent with the unsteady results, slight differences are due to the fact that the ring is not moving. The differences between the various simulations on the trajectory of the ring is also shown qualitatively in Fig. 8. On the left fully coupled (grey) and forced motion (blue) results are shown. The right side highlight the effect of the shock interation between coupled results (grey) and results without cylinder (red).

The flight mechanic simulation using the measured aerodynamic loads was intended to check the consistency of the experimental data set and the 6-DoF solver. Position, orientation and the corresponding velocities of the ring versus time are plotted in Fig. 10. The calculated curves (dashed lines) show good agreement and are largely within the error range of the measured data. The sensitivity of the motion state have been investigated including the given upper and lower error of the forces and moments (diamonds in Fig. 9) in the 6-DoF simulation. The results are within the blue areas. The errors add up over time and are therefore significantly larger than the errors of the direct measured values. The computed pitch angle and pitch rate are almost everywhere within this error range, which is not the case for the horizontal and vertical translational motion.

Figure 11 shows a series of simulation results of the coupled CFD/RBD simulation. Shown is the distribution of the surface pressure coefficient C_p and a schlieren image reconstructed from the density gradient in the center plane of the

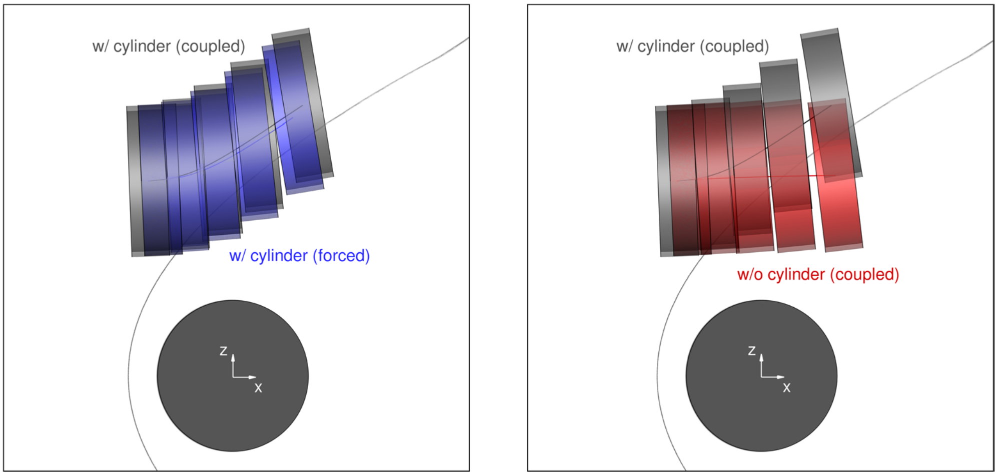

Fig. 8 Difference in position and attitude of the ring between coupled (grey) and forced motion (blue) simulation results (left). The force motion results are identical to the measured VKI Longshot data. Influence of the shock interaction on the position an attitude of the ring (right). Shown are the initial position at 3.8ms and results at 5.0ms, 7.0ms, 9.0ms, 11.0ms, and 13.0ms

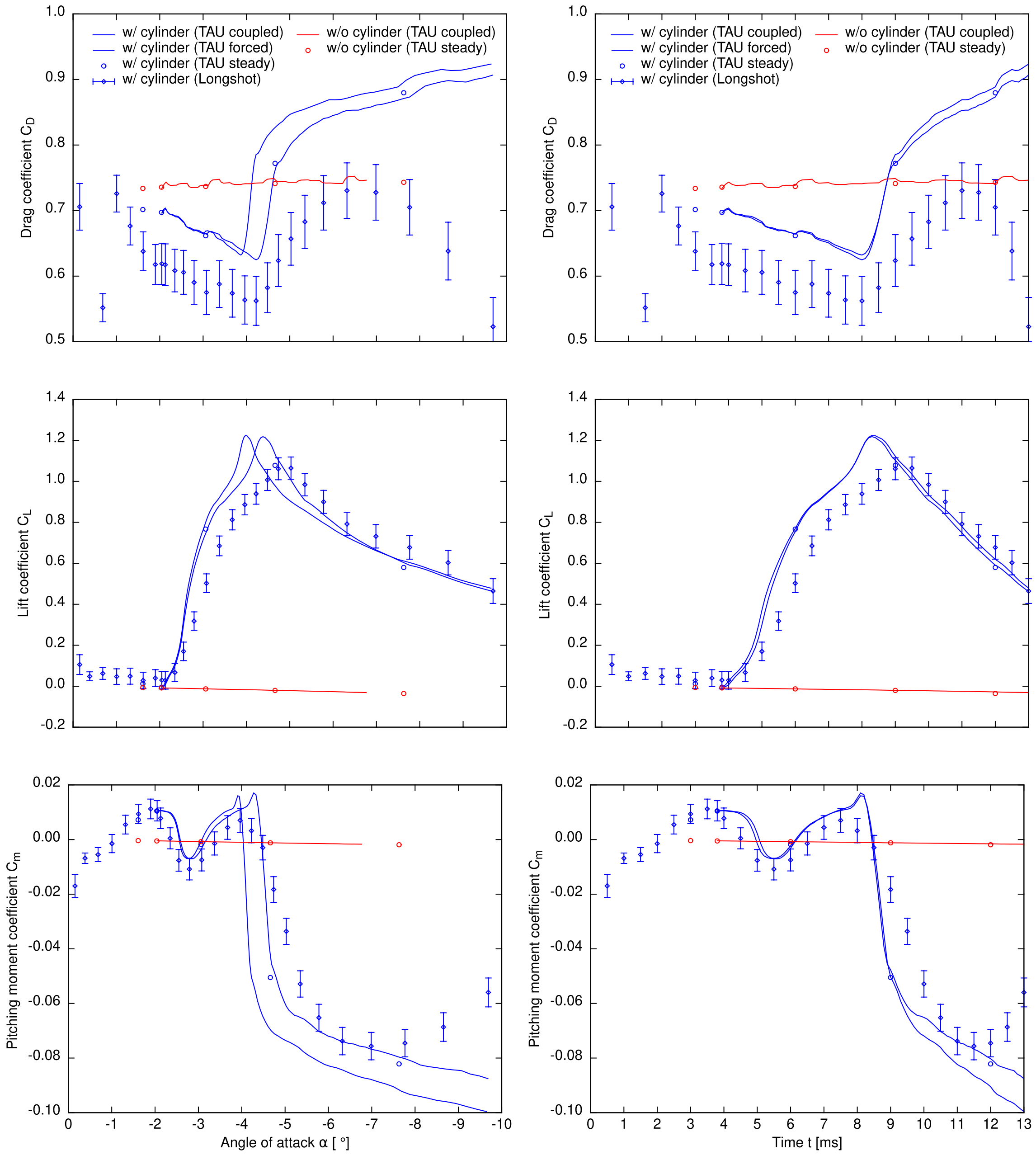

Fig. 9 Comparison of simulated (lines) and measured (diamonds) aerodynamic coefficients of the annular ring interacting with the bow shock in front of the cylinder (blue) and without shock interaction (red). Shown are results received with CFD/RBD coupling (solid lines) and forced motion results (dashed lines). The steady-state results (circles) have been simulated at a fixed time using the conditions at 3.0ms, 3.8ms, 6.0ms, 9.0ms, and 12.0ms (left to right) after flow onset

computational domain. In hypersonic flow the majority of the force is pressure-induced, so the C_p distribution is an indicator for the forces. As far as the ring is within the shock layer of the cylinder the interaction between the cylinder shock and the ring shock leads to a growing region of high pressure on the lower outer side of the ring which is responsible of the lift increases up to $t = 8.3$ ms. At this time the secondary interaction point reaches the stagnation region of the ring. The observed Edney type interaction increase the pressure on the thin front side of the ring up to a maximum value of $C_p \approx 6$. This pressure rise initiates the increase of the drag and the pitch down motion. When the interaction moves upwards, the pressure on the outer side and thus the lift decreases again.

6 Conclusion

Fully coupled CFD/RBD and forced motion simulations have been carried out to reproduce the VKI experiment of a free-flying ring crossing the curved shock wave in front of a cylinder. Both simulations show too high values for lift and drag compared to the measurements. The simulations also show a faster change of these values and can not reproduce the drag decrease and the pitching moment increase towards the end of the test time. One source for the less pronounced gradients could be the filtering of the experimental data. A Savitzky-Golay filter has been applied to the data. Not clear is if the filtering is also responsible for the bending of the curves at the end. Fact is that the ring leaves the core flow of the VKI Longshot nozzle and interacts with the shear layer [2], which should account for the majority of the effect. The

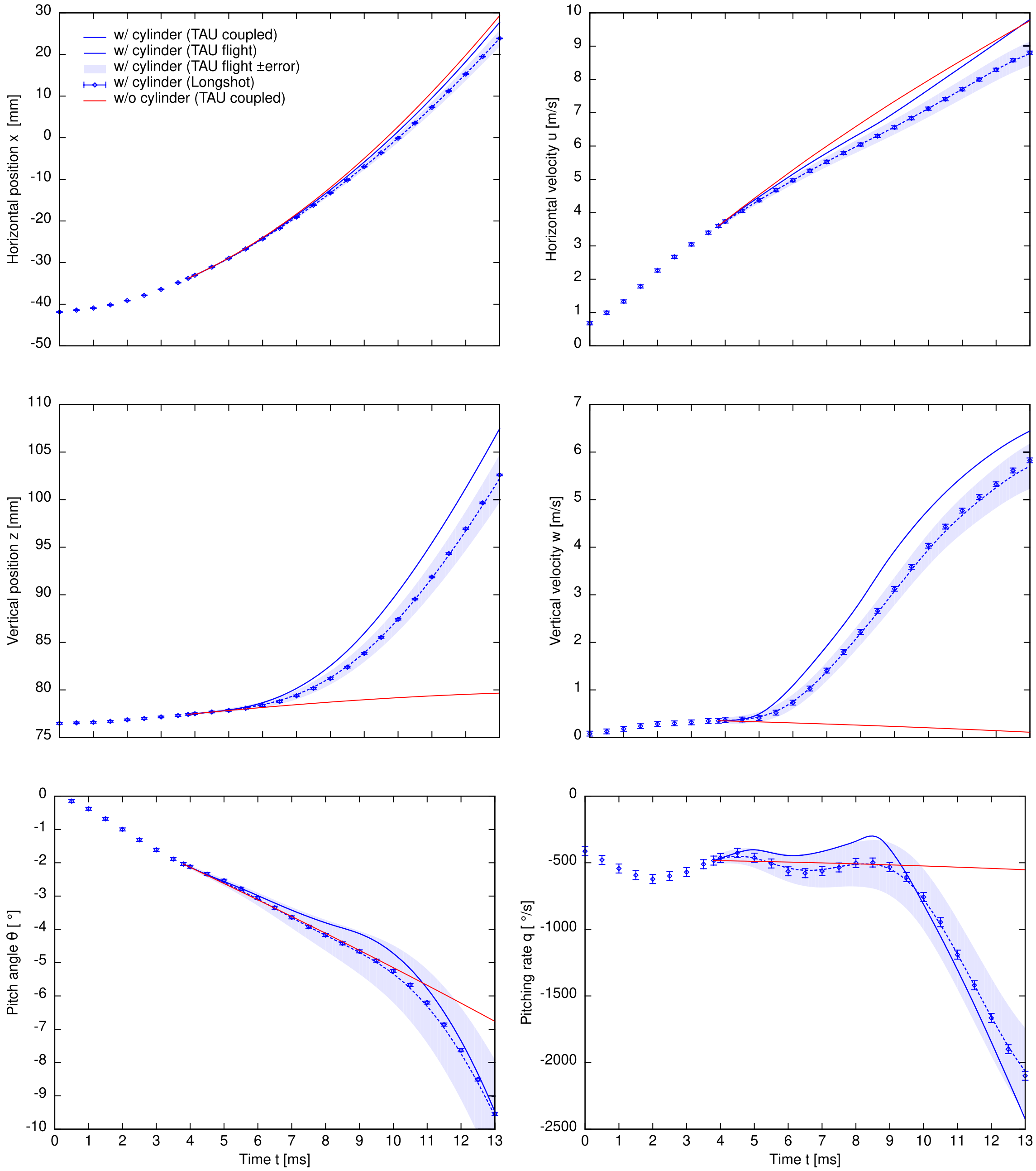

Fig. 10 Comparison of the simulated (lines) and measured (diamonds) motion state of the annular ring interacting with the bow shock in front of the cylinder (blue) and without shock interaction (red). Shown are results achieved with CFD/RBD coupling (solid lines) and results achieved with the flight mechanic solver and prescribed loads (dashed lines). In addition, flight mechanic results along the upper and lower error limits of the prescribed loads are shown (blue area)

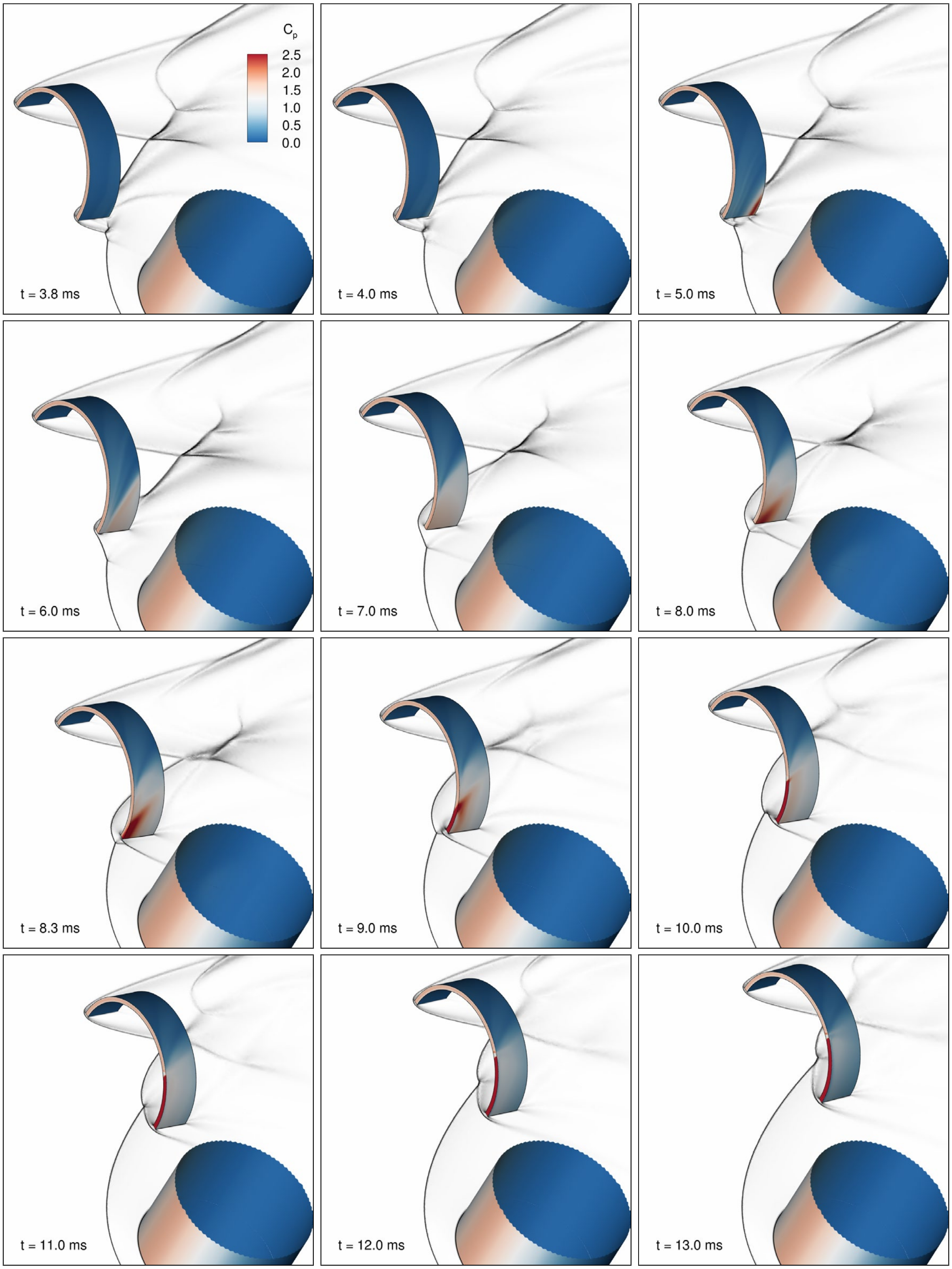

Fig. 11 Computed surface pressure coefficient C_p and center plane schlieren pictures showing the motion of the ring and the interaction between the shock waves. The results have been achieved with the coupled CFD/RBD simulation. The simulated time is from $t = 3.8$ ms (initial solution) to 13 ms. Maximum lift is reached at $t = 8.3$ ms. The maximum reached pressure coefficient is about $C_p \approx 6$

higher force values may be caused by different free stream values in the wind tunnel test and in the simulations or an inadequate gas model. A calorically perfect gas model is applied, neither thermo-chemical excitation of the nitrogen molecules in the nozzle reservoir nor freezing during the expansion process are taken into account. Some aspects of the calibration and the modeling of the Longshot nozzle expansion including the effects of non-perfect and dense gas corrections are discussed in [10] and [11]. The fact that the experimental data set is based only on one single experiment is not optimal, data from several experiments would allow to estimate the shot to shot variation regarding the initial and boundary (free stream) conditions.

Acknowledgements The author gratefully acknowledges the TAU code development team at the German Aerospace Center (DLR), as well as the scientific support and HPC resources provided by DLR. The HPC system CARA is partially funded by the Saxon State Ministry of Economic Affairs, Labour and Transport and the Federal Ministry of Economics and Climate Protection.

Author Contributions only one author

Funding Open Access funding enabled and organized by Projekt DEAL.

Data Availability No datasets were generated or analysed during the current study.

Declarations

Competing interests The authors declare no competing interests.

Open Access This article is licensed under a Creative Commons Attribution 4.0 International License, which permits use, sharing, adaptation, distribution and reproduction in any medium or format, as long as you give appropriate credit to the original author(s) and the source, provide a link to the Creative Commons licence, and indicate if changes were made. The images or other third party material in this article are included in the article's Creative Commons licence, unless indicated otherwise in a credit line to the material. If material is not included in the article's Creative Commons licence and your intended use is not permitted by statutory regulation or exceeds the permitted use, you will need to obtain permission directly from the copyright holder. To view a copy of this licence, visit http://creativecommons.org/licenses/by/4.0/.

References

1. Kovács, D.G., Grossir, G., Chazot, O.: Hypersonic aerodynamics of a free-flying ring interfering with a two-dimensional curved shock wave—an experimental test case. In: 2nd International Conference on Flight Vehicles, Aerothermodynamics, and Re-entry Missions and Engineering (FAR 2022), Heilbronn, Germany, 19–23 June (2022)
2. Kovács, D.G., Grossir, G., Chazot, O.: Space debris interaction across a two-dimensional oblique shock wave. Exp. Fluids **64**(146) (2023). https://doi.org/10.1007/s00348-023-03686-9
3. Grossir, G., Dias, B.: Flow characterization of the VKI Longshot wind tunnel. In: Flow Characterization and Modeling of Hypersonic Wind Tunnels. STO-AVT 325, pp. 1–32. von Karman Institute for Fluid Dynamics, Rhode-St-Genése, Belgium (2018)
4. Schwamborn, D., Gerhold, T., Heinrich, R.: The DLR TAU-Code: recent applications in research and industry. In: 4th European Conference on Computational Fluid Dynamics (ECCOMAS ECFD 2006), Eggmond aan Zee, The Netherlands, 5–8 September (2006)
5. Mack, A., V., H.: Validation of the unstructured DLR-TAU-code for hypersonic flows. In: 32nd AIAA Fluid Dynamics Conference and Exhibit, St. Louis, MO, USA, 24–28 June (2002). https://doi.org/10.2514/6.2002-3111
6. Madrane, A., Raichle, A., Stürmer, A.: Parallel implementation of a dynamic overset unstructured grid approach. In: European Congress on Computational Methods in Applied Sciences ans Engineering (ECCOMAS 2004), Jyväskylä, Finland, 24–28 July (2004)
7. Spiering, F.: Development of a fully automatic chimera hole cutting procedure in the dlr tau code. In: Dillmann, A., et al. (eds.) Notes on numerical fluid mechanics an multidisciplinary design, vol. 132, pp. 585–595. Springer, Cham (2016). https://doi.org/10.1007/978-3-319-27279-5_51
8. Heinrich, R., Reimer, L., Michler, A.: Multidisciplinary simulation of maneuvering aircraft interacting with atmospheric effects using the DLR TAU code. In: RTO AVT-189 Specialists' Meeting on Assessment of Stability and Control Prediction Methods for Air and Sea Vehicles, Portsdown West, UK, 12–14 October (2011)
9. Reimer, L., Heinrich, R., Meurer, R.: Validation of a time-domain TAU-flight dynamics coupling based on store release scenarios. In: Dillmann, A., et al. (eds.) Notes on numerical fluid mechanics an multidisciplinary design, vol. 124, pp. 455–463. Springer, Cham (2014). https://doi.org/10.1007/978-3-319-03158-3_46
10. Kovács, D.G., Ilich, Z., Grossir, G., Chazot, O.: Experimental characterization of the VKI longshot mach 14 contoured nozzle. In: 32nd AIAA SciTech Forum 2022, San Diego, CA, USA, 3–7 January (2002). https://doi.org/10.2514/6.2022-1401
11. Geratz, M., Capriati, M., Grossir, G., Magin, T.E.: Influence of physical models on the numerical modeling of hypersonic nozzle flow expansion. In: 9th European Conference for Aeronautics and Space Sciences (EUCASS), Lille, France, 27 June–1 July (2002). https://doi.org/10.13009/EUCASS2022-6142

Publisher's Note Springer Nature remains neutral with regard to jurisdictional claims in published maps and institutional affiliations.